ACS NANO

www.acsnano.org

Article

# Structural and Compositional Evolution of Colloidal $In_{1-x}Ga_xP_{1-y}As_y$ Nanocrystals during Cation Exchange Revealed by Electron Microscopy

Benjamin F. Hammel, Zirui Zhou, Justin C. Ondry, Dmitri V. Talapin, Sadegh Yazdi, and Gordana Dukovic*

Cite This: https://doi.org/10.1021/acsnano.5c15614

Read Online

ACCESS | Metrics & More | Article Recommendations | Supporting Information



**ABSTRACT:** Cation exchange in molten salts has emerged as a method to synthesize colloidal III–V quantum dots with tunable composition and excellent optoelectronic properties. However, the atomistic details of how cation exchange occurs and the elemental distribution in the products remain elusive. In this work, we use scanning transmission electron microscopy to reveal the chemical and structural evolution of $In_{1-x}Ga_xP_{1-y}As_y$ nanocrystals made by cation exchange of $InP_{1-y}As_y$ nanocrystals in a gallium-containing molten salt. The starting material and $In_{1-x}Ga_xP_{1-y}As_y$ nanocrystals at multiple time points in the reaction were characterized by aberration-corrected HAADF-STEM and STEM-EDS. HAADF-STEM reveals subtle changes in size and shape, but the tetrahedral morphology and zinc-blende crystal structure are maintained throughout the reaction. We overcome the technical challenges of beam damage and low signals in STEM-EDS through a combination of experimental optimization and image processing to yield elemental composition maps representative of individual nanocrystals. This analysis revealed that the particles have Ga-rich surfaces at the early reaction stage. As the reaction proceeds, Ga permeates the lattice, but the elemental distribution remains graded with In enrichment in the core even after 16 h. To investigate the origin of the observed elemental distributions, we use finite element analysis to model the cation exchange as a diffusion-limited process, which suggests that cation exchange becomes progressively more difficult as In atoms are replaced by Ga. We discuss the implication of the graded composition on optical properties. More broadly, the image processing techniques developed here could be applied to other compositionally complex nanocrystals.

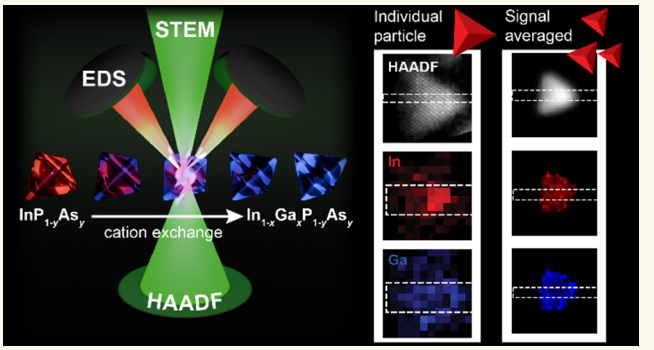


**KEYWORDS:** *cation exchange, nanocrystal, molten salt, scanning transmission electron microscopy, energy-dispersive X-ray spectroscopy, high-angle annular dark field imaging, finite element analysis*

Colloidal semiconductor nanocrystals (NCs) offer remarkable tunability in electronic structure and optical and chemical properties enabled by synthetic control of particle size, shape, and composition. Incorporating multiple elements into a semiconductor NC introduces additional degrees of freedom in the structure and properties. While a binary semiconductor NC has a fixed lattice parameter and related electronic structure, ternary and quaternary semiconductors can be designed to provide independent control of lattice parameter, band gap, and size, offering a fine degree of control applicable to high-performance optoelectronic devices.[1] However, in compositionally complex NCs, atoms of different elements can arrange themselves in different ways, from a completely homogeneous distribution to core/shell heterostructures and compositional gradients in between.[2−5] These different elemental distributions play an important role in optoelectronic properties.[6,7] Famously, core–shell NCs have been used with remarkable success to reduce carrier trapping and funnel excitons to the core, resulting in bright photoluminescence.[8−14] Moreover, compositionally graded interfaces have been an emerging design strategy for improved photoluminescence properties of II–VI NCs.[15−19] Therefore, synthetic control of elemental distribution in compositionally complex NCs is an essential requirement for controlling NC optical properties.[17,19−22]

A remarkable example of compositional complexity in NCs is the variety of III–V solid solutions that can be synthesized at high temperatures in molten salts, yielding materials with

Received: September 10, 2025
Revised: January 26, 2026
Accepted: January 27, 2026

potential applications in photonics, photocatalysis, and quantum information science.[23−30] A range of III−V compositions can be accessed by annealing indium pnictides in Ga and Al molten salt baths.[28] Critical to understanding these molten salt transformations is the question of how the original NC lattice is transformed to the final product. The cation exchange reaction in each particle requires the transport of cations in ($Ga^{3+}$/$Al^{3+}$) and out ($In^{3+}$) of the lattice. One may expect that the elemental distribution would evolve from exchange at the surface to an alloyed phase, with potentially concurrent strain and lattice distortions.[24,25] The elemental distribution is critically related to optoelectronic properties, given that a homogeneous distribution is likely to have different optical properties in comparison to a core/shell or graded distribution. However, ensemble techniques like powder X-ray diffraction (PXRD) and solid-state nuclear magnetic resonance (NMR) are not sufficiently sensitive to reveal such structural and compositional details and cannot reveal single-particle details in an ensemble with non-negligible heterogeneity.[24,26]

In this article, we examine the transformation of $InP_{1-y}As_y$ to $In_{1-x}Ga_xP_{1-y}As_y$ NCs with scanning transmission electron microscopy (STEM) to reveal structural and compositional information across individual NCs over the course of the reaction. We characterize the $InP_{1-y}As_y$ starting material and $In_{1-x}Ga_xP_{1-y}As_y$ NCs made by annealing $InP_{1-y}As_y$ NCs in a molten salt for four different time points in the reaction (Figure 1), allowing us to track the progress of the cation exchange. High-angle annular dark field (HAADF)-STEM imaging reveals that surface facets reconstruct and the atomic lattice contracts during molten salt annealing, while the zinc-blende crystal structure is maintained. We used energy-dispersive X-ray spectroscopy (STEM-EDS) to characterize the elemental composition of the NCs. The small NC size leads to limited signal-to-noise ratios and beam-induced damage, which, in turn, lead to a limited ability to resolve elemental distributions within individual NCs. To address this problem, we aggregated the signal from multiple particles to generate single-particle elemental distributions. To our knowledge, this is the first time that such an analysis has been used for semiconductor NCs.[31−33] Our analysis finds that the compositional change is rapid at the start of the reaction and then slows significantly. Concurrently, early in the reaction, we observe Ga enrichment on the surface and In enrichment in the core. This composition gradient decreases as the reaction proceeds but does not reach homogeneity. Numerical simulations suggest that the diffusion coefficient must decrease as the reaction proceeds to describe the experimental results.

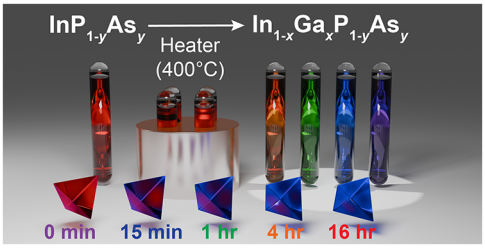


**Figure 1.** Schematic of molten salt cation exchange as previously described by Ondry et al.[28] Quartz ampules, containing NCs dispersed in a salt matrix, are heated in parallel in a reactor, causing $Ga^{3+}$ in the molten salt to exchange with $In^{3+}$ in the NCs.

We discuss the potential origins of the composition-dependent diffusion coefficient and the implications of the graded composition on the optoelectronic properties of $In_{1-x}Ga_xP_{1-y}As_y$ NCs. Overall, electron microscopy reveals structural changes at the surface and the emergence of a composition gradient from diffusion-limited cation exchange. This insight may inform the fundamental understanding of diffusion processes in nanoscale crystals as well as the synthesis of compositionally complex III−V NCs toward improved control of optoelectronic performance. More broadly, the analysis described herein can be applied to a wide range of compositionally complex nanomaterials.

## RESULTS AND DISCUSSION

### NC Size, Shape, and Composition Changes over the Course of Molten-Salt Annealing

In this work, we studied the transformation of $InP_{1-y}As_y$ NCs to $In_{1-x}Ga_xP_{1-y}As_y$ NCs via molten-salt annealing. We selected 5 samples: the $InP_{1-y}As_y$ starting material and four $In_{1-x}Ga_xP_{1-y}As_y$ NCs that were annealed in gallium-containing molten salts for 15 min, 1, 4, and 16 h (Figure 1). We examined the structural evolution of the NCs using HAADF-STEM imaging, as shown in Figure 2. To determine the morphology and size of the particles, we acquired large field of view HAADF-STEM images containing hundreds of particles, as shown in Figure 2a, with representative magnified insets shown in Figure 2b. In the HAADF-STEM images, the $InP_{1-y}As_y$ NCs resemble tetrahedrons, and the $In_{1-x}Ga_xP_{1-y}As_y$ NCs maintain their tetrahedron shape throughout the molten salt exchange. We quantified the size and shape of the NCs as described in Section 1 (SI) (Figure S1 and Table S1). We observe a gradual increase in diameter of ∼1 nm over the first 4 h of the exchange; an increase in size was also observed by TEM in prior work on molten salt annealing and will be addressed later.[30] There is a slight decrease in size after 16 h, and the standard deviation of the size increases after 4 and 16 h of annealing, which was also previously observed by X-ray techniques and suggests that the NCs begin to decompose after long annealing times.[25] Between the starting $InP_{1-y}As_y$ and the $In_{1-x}Ga_xP_{1-y}As_y$ annealed for 15 min, there is an abrupt decrease in circularity, a metric for shape (see Figure S1, and surrounding discussion for details). Annealing for longer times results in a minimal change in circularity (Figure S1). The circularity analysis suggests that, within the first 15 min of annealing, the surface of the starting material reconstructs to form more well-defined {111} tetrahedral facets. In fact, it was previously observed that in molten salt baths, InP spheres can transform into $In_{1-x}Ga_xP$ tetrahedrons.[24] These morphological changes illustrate how actively the surface can reconstruct during molten salt annealing.[24] In the current case, the subtle changes in size and shape point to the importance of transformations at the particle surface, which we will discuss in relation to compositional changes.

To examine the average composition changes throughout the molten-salt annealing process, we simultaneously acquired STEM−EDS maps in the same regions where we collected large field-of-view HAADF-STEM images, as shown in Figure 2a. These large maps are summed into the EDS spectra shown in Figure 2c. To account for differences in absolute intensity due to variation in factors such as the amount of material in the mapping region and the electron dose, the EDS intensities are normalized to the intensity of the As-L$\alpha$ peak. Figure 2c shows


https://doi.org/10.1021/acsnano.5c15614
ACS Nano XXXX, XXX, XXX−XXX

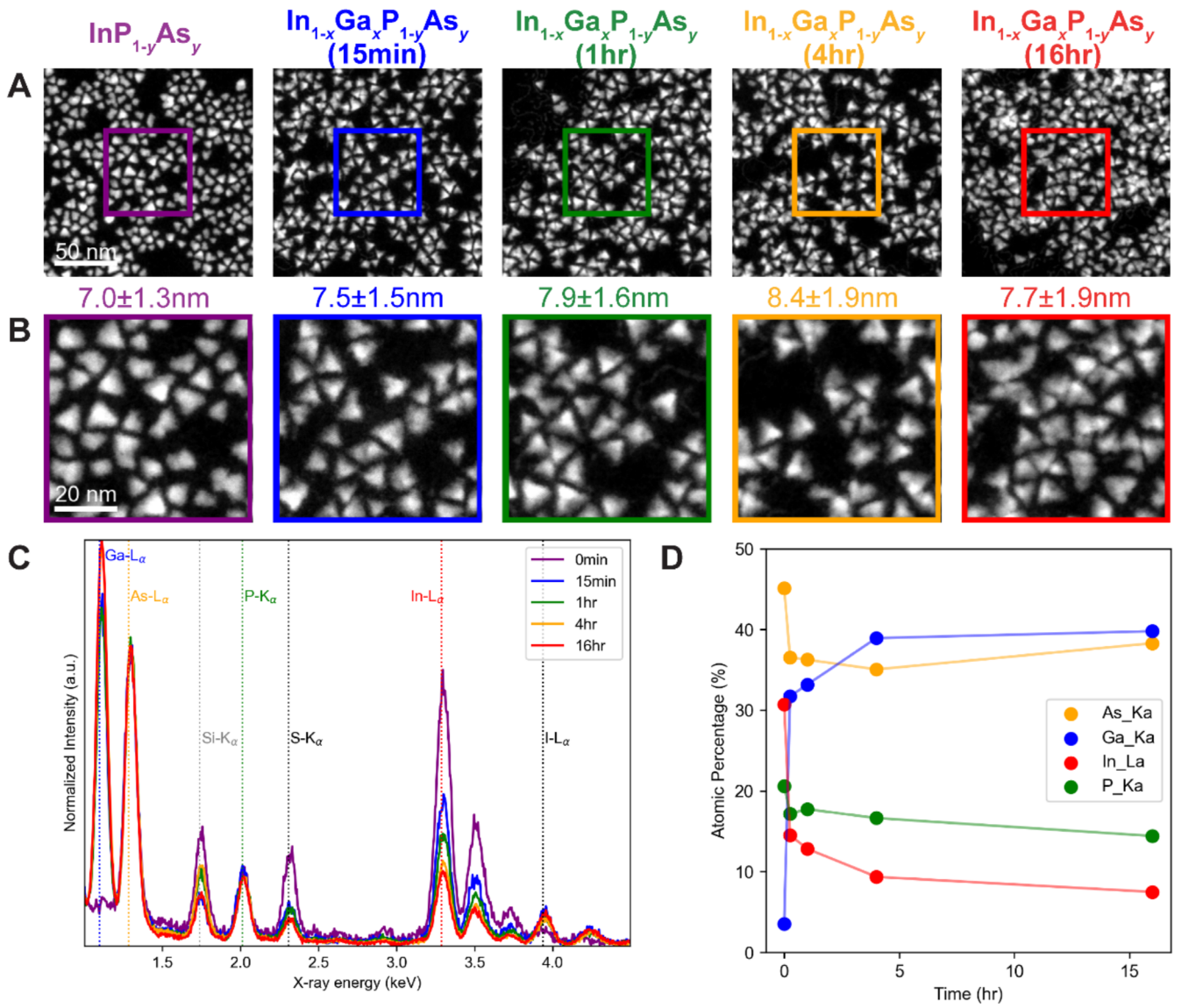


**Figure 2.** (A) Large field-of-view HAADF-STEM images from each sample in the $In_{1-x}Ga_xP_{1-y}As_y$ reaction series. (B) Magnified insets of images from the regions marked with squares. The mean diameter and standard deviation, measured by taking the peak position and standard deviation of the distribution with a Gaussian fit (Figure S1), are shown in between the images and the insets. (C) EDS spectra obtained from the entire region shown in (A). Spectra are normalized at the As-L$\alpha$ edge and overlaid to highlight relative changes in peak intensity. (D) Elemental quantification from EDS spectra.

the energy range from the Ga-L$\alpha$ to the I-L$\alpha$ peaks, which shows peaks corresponding to expected elements (Ga-L, As-L, P-K, In-L), peaks that commonly appear in the EDS spectra regardless of the sample (Si-K from the EDS detector), and some additional peaks (S-K, I-L). We performed a series of EDS experiments to understand the origin of all of these peaks, which is described in detail in the SI (Section 2, Figures S2–S8, Table S2, and related discussion). Here, we focus on Ga, As, P, and In. The most striking feature in Figure 2c is that the Ga peaks reach over 50% of their maximum intensity after just 15 min of annealing. This rapid appearance and growth of the Ga peaks illustrate the dramatic composition change that occurs early in the reaction. The rise of the Ga-L peak is accompanied by a decrease in the In-L peak intensity. The relative intensities of the As-L and P-K peaks are effectively constant. This is to be expected from a cation-exchange reaction, where $Ga^{3+}$ replaces $In^{3+}$ atoms, while the anion composition does not change. As the samples anneal for longer periods of time, the cation exchange continues: the Ga-L peak continues to rise, the In-L peak falls, and the As-L and P-K peaks remain constant. There is still an In-L peak after 16 h of annealing, indicating that Ga has not completely exchanged with In. The optical properties of the NCs are consistent with these compositional changes. The apparent band gap blue shifts with Ga incorporation (Figure S9) as expected because Ga-containing III–V semiconductors have larger band gaps than In-containing III–V semiconductors with the same anions.[28] Furthermore, the apparent exciton peak in the $InP_{1-y}As_y$ QD sample appears to go away with $Ga^{3+}$ exposure (Figure S9). This is reminiscent of the changes seen for the molten-salt conversion of InP QDs to $In_xGa_{1-x}P$, which were attributed to a transition from a direct semiconductor to an indirect one.[26]


https://doi.org/10.1021/acsnano.5c15614
ACS Nano XXXX, XXX, XXX–XXX

EDS intensities provide a qualitative measure of composition; to understand quantitative changes in composition, we performed elemental quantification on the EDS spectra using the Cliff–Lorimer method (see Section 4 (SI) and Table S3 for details). In Figure 2d, we plot the quantification results for the regions of particles shown in Figure 2a, which roughly contain 200 particles each. As seen already, the Ga concentration rises concurrently as the In concentration falls. Remarkably, as noted above, most of the change in composition happens within the first 15 min of annealing. The In concentration drops in half, from roughly 30% to 15%, between the $InP_{1-y}As_y$ sample and the 15 min reaction sample, while the Ga concentration increases to ∼30%. This rapid change in composition is followed by slower changes in composition in the subsequent samples; the cation exchange is not complete even after 16 h. It is also interesting that the magnitude of the decrease in the In concentration (15%) does not match the magnitude of the increase in the Ga concentration (30%). In the same time frame, the anion concentration decreases. These changes in composition reflect an abrupt increase in the cation-to-anion ratio between the starting $InP_{1-y}As_y$ NCs and the cation-exchanged $In_{1-x}Ga_xP_{1-y}As_y$ ones (see Section 4 (SI) and Figure S10). We considered whether these changes were due to inaccuracies in the EDS quantification method. However, the magnitude of the changes is beyond what we would expect for experimental inaccuracies (Section 4 (SI)). Moreover, X-ray fluorescence data previously collected on the same samples show a similar trend.[28]

We posit that the increase in the cation-to-anion ratio between the first two samples is caused by the addition of Ga to the surface. Prior to molten salt annealing, the native organic ligands of the $InP_{1-y}As_y$ starting material are exchanged with gallium halide ligands.[28] During the molten salt annealing, the NCs are exposed to a bath of gallium halide species.[28] During both steps, the surface could become decorated with Ga species, and because of the high surface-to-volume ratio of NCs, this Ga on the surface would induce a substantial change in the overall composition of the NCs; we estimate that a monolayer could contribute as much as 20% of the total composition (see Section 5 (SI) and Figure S11), in line with previous estimates.[34] This deposition of Ga cations would also explain the overall increase in the particle size, as seen in Figure 2. The outsized contribution of the surface to the composition of III–V NCs has been recognized in prior work on molten salt cation exchanges, particularly when comparing the composition extracted from inductively coupled plasma-optical emission spectroscopy (ICP-OES) and X-ray fluorescence (XRF) versus PXRD; the composition from ICP-OES or XRF often has more Ga than the composition from PXRD, and this discrepancy is attributed to Ga on the surface that does not significantly perturb the entire lattice of the nanocrystal.[24−26] An important distinction is that, during previous work, the Ga on the surface was thought to originate from rapid exchange with In.[25] The shift in the cation-to-anion ratio within the first 15 min of the reaction (Figure S10) suggests that, in addition to rapid surface exchange, a significant amount of Ga is *added* to the surface. These composition changes and the morphological changes described above (Figure 2a,b) highlight how actively the surface changes during the initial stages of molten salt annealing.

Annealing for longer periods of time results in less dramatic composition changes. The In/Ga cation exchange continues gradually for the sample annealed for 1 and 4 h, while annealing for 16 h barely changes the composition (Figure 2d). The initially rapid but later slow composition changes have been previously observed by ensemble characterization (PXRD, ICP-OES, and XRF) of $In_{1-x}Ga_xP$ and $In_{1-x}Ga_xAs$ NCs formed, respectively, from cation exchange of InP and InAs NCs.[24,25] From that prior work, it is notable that the rate of exchange is orders of magnitude faster than expected from bulk.[24,25] However, despite the initially fast exchange, the exchange rarely reaches completion (100% Ga). Rather, the final composition following several hours of annealing depends on the reaction temperature. For example, the samples studied here were annealed at 400 °C and have a final ensemble composition of 73% Ga,[28] while recent work suggests that temperatures of 450 °C and higher are necessary to produce $In_{1-x}Ga_xAs$ with Ga contents above 80%.[30] The factors that govern the overall composition changes are not understood. This motivated us to investigate how the structure within the nanocrystal evolves with molten salt annealing, with the aim of revealing mechanistic details about the reaction.

## Crystal-Structure Evolution during Molten-Salt Annealing

We used aberration-corrected HAADF-STEM images (Figure 3a) to resolve the atomic structure of the NCs and explore how cation exchange influences the local crystal structure. During TEM sample preparation, NCs randomly orient on the grid, occasionally on a zone axis. We observe that many NCs appear in an asymmetric orientation, which we determined, using models and HAADF-STEM simulations (Figure 3b), to be the ⟨110⟩ zone axis, as discussed in more detail in the SI (Section 6 and Figures S12–S15). We focused our attention on NCs oriented along the ⟨110⟩ zone axis (Figure 3a); in this orientation, the atomic columns are spatially well-separated and chemically distinct—columns contain either all cations or all anions—both of which make this orientation relatively easy to image and interpret. For example, we can fit the fast Fourier transform (FFT) of the images and orient them based on their crystal structure (Section 7 (SI) and Figure S16). By analyzing NCs oriented in the same direction, we can more easily compare the atomic structure and elemental distribution between reaction time points.

With the atomic-resolution images in Figure 3, we see that a coherent zinc-blende structure is maintained throughout the reaction. This is consistent with prior PXRD and Raman results.[28] Thanks to the high crystallinity of these samples, the atomic "dumbbells" expected from the model (Figure 3b) are observed in the experimental images (Figure 3a, magnified inset). For the $InP_{1-y}As_y$ sample, the ends of the dumbbells have different intensities because the left column contains P/As while the right column contains In, and the atomic number of In is greater than that of P/As. We observe that the difference in the intensities of the atoms in the dumbbell decreases with annealing time. This is evidence that the In is being replaced with Ga since Ga and As have similar atomic numbers, resulting in a similar HAADF intensity. Interestingly, we notice that the brighter, cation end of the dumbbell always faces the thick end of the tetrahedron; this reflects selective stabilization of the {111} facets over {−1−1−1} facets, as described in the SI (Figure S12 and surrounding discussion). The preferential stabilization of {111} facets is consistent with reports on tetrahedral InP NCs, where the {111} facets are described as cation-terminated and the {−1−1−1} as anion-terminated; when passivated by ligands, the {111} facets are


https://doi.org/10.1021/acsnano.5c15614
ACS Nano XXXX, XXX, XXX−XXX

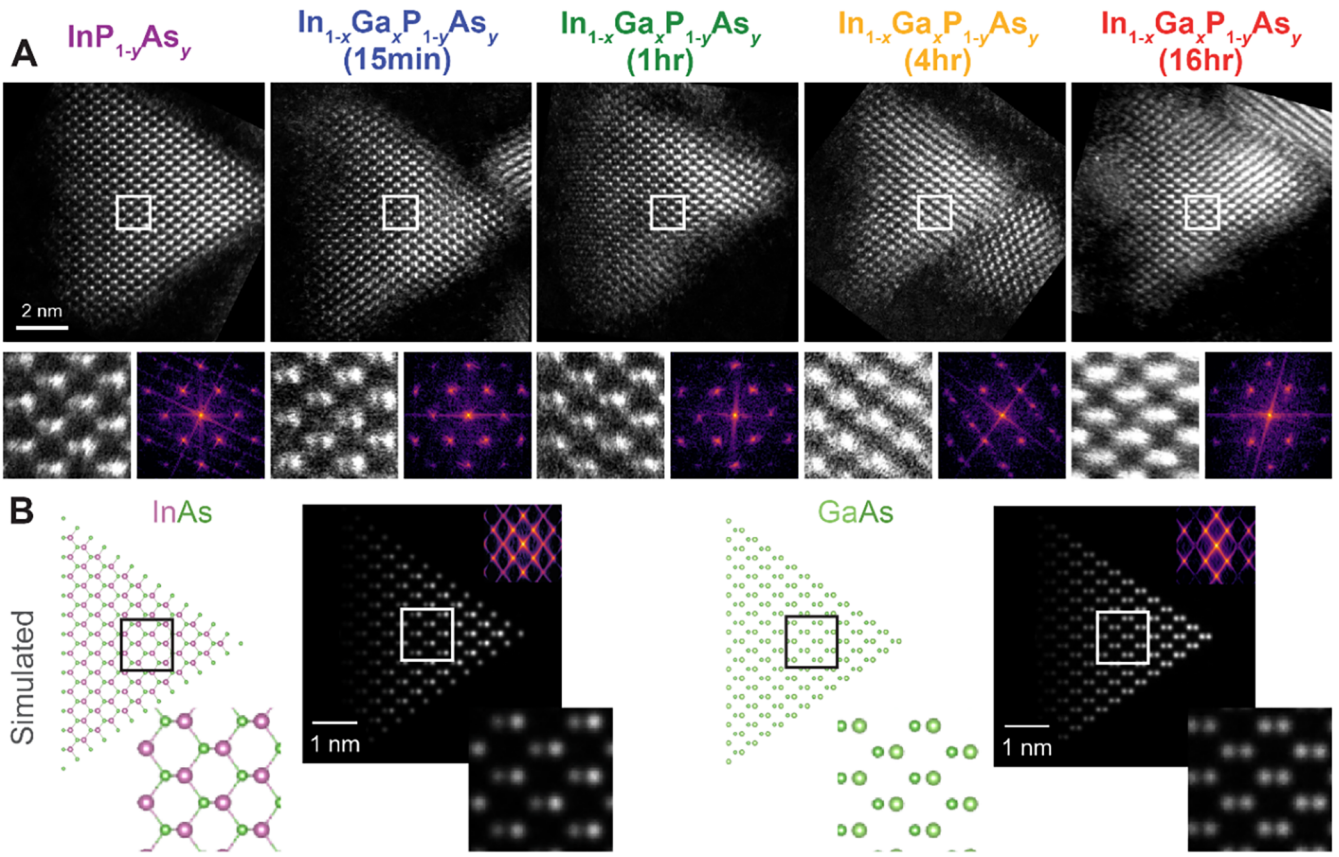


**Figure 3.** (A) High-magnification HAADF-STEM images from each sample in the $In_{1-x}Ga_xP_{1-y}As_y$ reaction series. Below, left are zoomed-in regions (indicated with the white box) of the image, followed by the FFT of the full images on the right. (B) Model and simulated HAADF-STEM images (inset FFT) of InAs and GaAs tetrahedrons oriented down the ⟨110⟩ zone axis. Zoomed-in regions (black or white boxes) highlight the dumbbells of the zinc-blende structure.

lower in energy than {−1−1−1} facets.[35−37] The preferential stabilization of cation-rich {111} facets is also consistent with our observation that the NCs become more sharply faceted and their surfaces are Ga-rich in the initial stages of molten salt annealing.

Due to the smaller size of Ga, we would expect that the lattice constant of the crystal would decrease as more Ga is incorporated. To determine the lattice constant of the particles produced at different stages of the reaction, we analyzed the FFT of the atomic-resolution images, as detailed in the SI (Section 7 and Figures S16 and S17). Shifts in the FFT peaks indicate an ∼2% contraction in the lattice, which is consistent with larger $In^{3+}$ cations being replaced by smaller $Ga^{3+}$ cations. Similar lattice contraction was observed in ensemble PXRD patterns (Figure S18),[28] indicating that the contraction observed in single NCs is representative of the ensemble. The HAADF-STEM images and their analysis show that the cation-exchange reaction maintains the crystal structure of the parent $InP_{1-y}As_y$ with the expected average lattice contraction when In is replaced with Ga. Now we turn to the critical question of how In and Ga are distributed in the $In_{1-x}Ga_xP_{1-y}As_y$ NCs.

If the cation exchange were to lead to an abrupt core−shell structure, it would be likely resolvable in HAADF-STEM images. In and Ga have atomic numbers and sizes that are different enough that we would expect to see local differences in the intensity and position of the atomic columns, especially in the case of an abrupt composition change. To investigate this, we performed extensive analysis of atomic-resolution HAADF images (see Section 8 (SI) and Figure S19). While we do observe some local changes in the intensity and lattice structure, we do not observe a clear interface in any of the NCs measured. This suggests that the composition distribution cannot be described as an abrupt core/shell structure but rather a diffuse profile. In principle, the composition distribution of the NCs could be determined by HAADF-STEM; the intensity of the atomic columns is correlated with their elemental composition, and from this orientation, the columns are two-component systems amenable to "atom-counting."[38,39] However, in practice, our HAADF-STEM analysis is limited by low numbers of atomic-resolution images, the precision of the measurements, and other confounding factors, such as varying thickness and crystalline defects, that complicate interpretation of the results (Figure S19). By comparison, STEM-EDS peaks are element-specific and well-separated in energy, providing an unambiguous determination of composition as a function of position. For that reason, we turn to STEM-EDS to measure the elemental distribution of the NCs.

## Single-Particle Elemental Distribution over the Course of Molten-Salt Annealing

In STEM-EDS, a high-energy electron beam is rastered across an area, resulting in the emission of characteristic X-rays whose energy is measured by the detector. Because this information is collected with a fine electron probe, STEM-EDS maps can be collected with atomic resolution.[40] However, STEM-EDS


https://doi.org/10.1021/acsnano.5c15614
ACS Nano XXXX, XXX, XXX−XXX

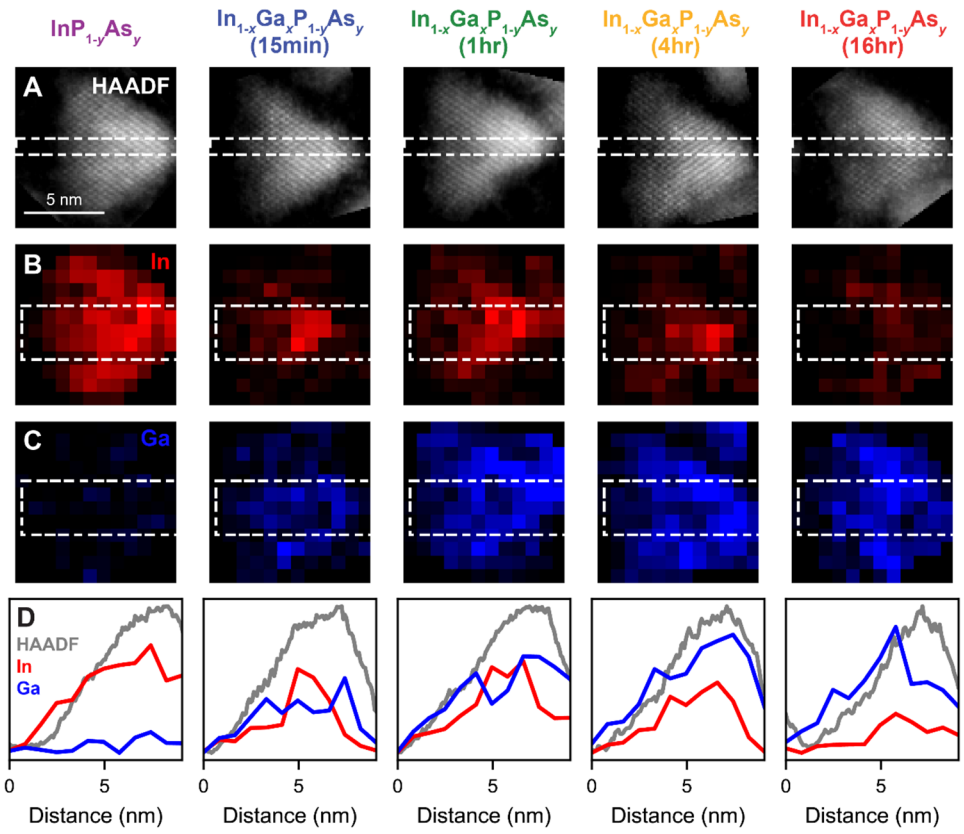


**Figure 4.** (A) HAADF-STEM and (B, C) STEM-EDS intensity maps for In and Ga, respectively, for each sample in the $In_{1-x}Ga_xP_{1-y}As_y$ reaction series. All five particles are oriented down the ⟨110⟩ zone axis and rotated to be in the same crystallographic direction. The HAADF images are from the first frame of the EDS acquisition. The signal intensity in EDS maps is background-subtracted, integrated, and normalized to the As-L$\alpha$ intensity. The EDS spectra are binned by a factor of 10. All images are at the same scale. (D) Line profiles taken from dashed white regions of (A–C).

mapping on semiconductor NCs is often a challenging proposition; their small size begets beam sensitivity and low scattering efficiency, resulting in low signal. To maximize the signal that can be extracted before the particles degrade, we surveyed accelerating voltage, beam current, cryo-cooling, and other microscope parameters to optimize the data collection. We ultimately found that lower accelerating voltages (80 kV), higher beam currents (>100 pA), and an ambient temperature holder with low shadowing gave the greatest signal per unit area (see SI, Section 9 and Figures S20–S23). We also found that using low magnification and large mapping areas minimizes the electron dose experienced by individual nanocrystals (see SI, Section 9 and Figure S24). Importantly, we verified that the changes to the local elemental distribution due to the electron beam were minimal by examining the EDS data throughout the course of the collection (see SI, Section 9 and Figures S25 and S26).

We then collected STEM-EDS data under these optimized conditions to evaluate the elemental distribution of the individual $In_{1-x}Ga_xP_{1-y}As_y$ NCs. Representative intensity maps qualitatively showing the elemental distribution as a function of molten salt exchange time are displayed in Figure 4. For ease of comparison, maps are shown from particles oriented on the same zone axis (⟨110⟩), as shown in the HAADF images in Figure 4a, and aligned based on their FFTs, as described in the SI (Section 7, Figure S16, and surrounding discussion). Although the particles are oriented along a zone axis, the effect of channeling on the EDS signal is likely negligible due to their small size.[41] The overall EDS intensity is correlated to the thickness, so it is important to note that particles oriented on the ⟨110⟩ zone axis are shaped like a wedge, increasing in thickness from left to right (Figure S15). The relative contribution of the core vs surface also depends on the orientation; in this orientation, the center of the particle, or the part furthest away from the surface, is biased to the right end, and the right edge also has the greatest contribution from the surface. As expected, the $InP_{1-y}As_y$ sample does not show the presence of Ga. In the $In_{1-x}Ga_xP_{1-y}As_y$ sample produced after 15 min of molten salt annealing, we see the appearance of the Ga signal, particularly near the particle edges, while the In signal is now concentrated in the particle core (Figure 4b–d). In other words, the composition is relatively Ga-rich at the edges and relatively In-rich at the center of the particle. As the cation exchange proceeds, the Ga concentration increases and exchanges with In deeper into the nanocrystal, resulting in a more uniform Ga-rich elemental distribution.

Ideally, we would collect enough signal on each individual particle to quantify the composition profile. However, the efficiency of STEM-EDS is limited by the low probability of inelastic collisions, the X-ray fluorescence yield (especially for light elements), and the limited collection efficiency of the STEM-EDS detectors. The low efficiency of STEM-EDS means that high electron doses are needed to collect high signals. For these samples, the electron doses required for a high EDS signal were well beyond the dose at which the


https://doi.org/10.1021/acsnano.5c15614
ACS Nano XXXX, XXX, XXX–XXX

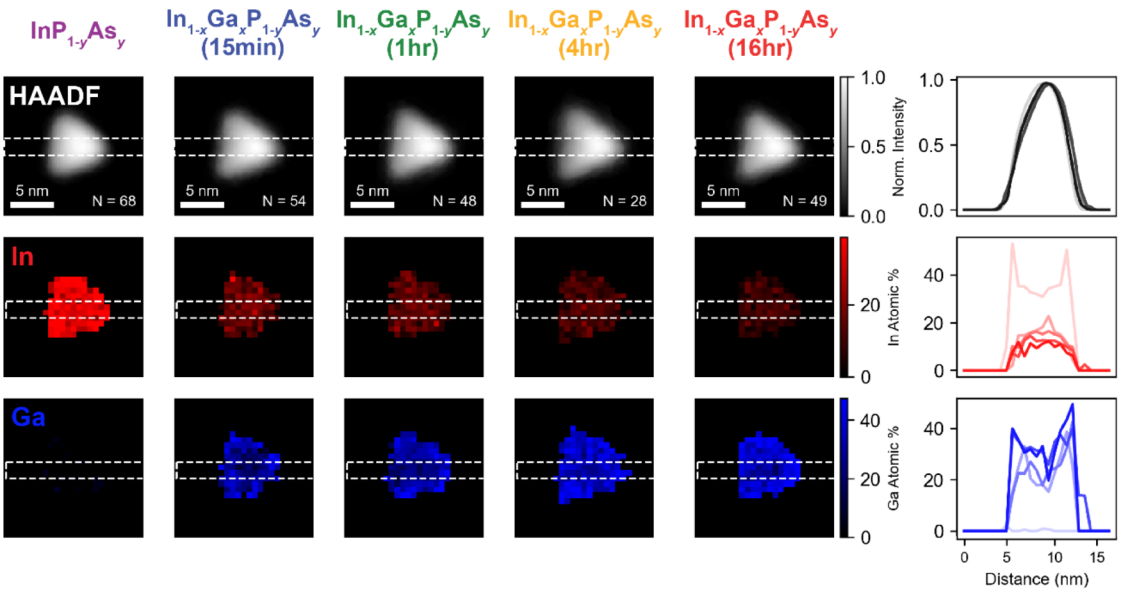


**Figure 5.** Top: aligned and summed HAADF images for each reaction time point. Middle and bottom: elemental distribution maps for In (red) and Ga (blue) obtained by summing EDS spectrum images of the particles at each reaction time point. The number of particles summed ("*N*") is shown in the bottom right corner of the HAADF image for each reaction time point. The line profiles are taken from left to right, summing over the area indicated by the dashed white lines. The opacity of the line increases with reaction time, with the $InP_{1-y}As_y$ sample shown with the lightest line and the $In_{1-x}Ga_xP_{1-y}As_y$ annealed for 16 h plotted with the darkest line.

particles would decompose. Even under the best conditions, the signal density from individual NCs was insufficient for high-resolution elemental quantification in individual particles. Therefore, we sought to use the EDS signal from many similar particles under a lower electron dose to make representative "single-particle" EDS maps, inspired by single-particle analysis methods employed in structural biology and, more relatedly, on metal NCs.[31−33,42−48]

We leveraged the open-source Python library *ParticleSpy* to automatically segment and classify hundreds of particles based on HAADF-STEM and then summed and analyzed the EDS data using the *HyperSpy* library.[49,50] In Figure 2, we demonstrated that we could simultaneously acquire HAADF-STEM and EDS spectral images over a large field of view, where each map contains hundreds of particles and is at a lower electron dose per particle than Figure 4. The high contrast of the particles in HAADF-STEM aids in identifying and segmenting the particles with *ParticleSpy*. Because there are hundreds of particles in the frame, the overall EDS spectrum contains thousands of counts, which can be spatially overlaid to give a map with a high signal. In Figure 3, we used atomic-resolution HAADF-STEM and modeling to understand the orientation of the particles. These methods help us overcome heterogeneity in size, shape, and orientation. Single particle analysis relies on the particles being virtually identical, which normally would preclude this analysis from being applied to most nanocrystal samples. However, from a heterogeneous ensemble of NCs, a homogeneous subset of particles can be selected that are valid for single-particle reconstruction.[32] From the HAADF-STEM images, we selected a relatively homogeneous set of particles. We filtered for size and shape by excluding particles within one standard deviation of the mean area and circularity (SI, Section 10 and Figure S27). The filtered particles were then oriented by rotating relative to a template and manually selecting particles oriented on the ⟨110⟩ zone axis (SI, Section 10 and Figure S28). These filtered particles were then selected for EDS analysis and signal averaging: we used the particle information from HAADF-STEM to crop out the EDS spectrum images and align the entire spectrum image rotationally. After performing these operations, summing the EDS spectrum images across dozens of particles, and binning the data further to increase the signal per pixel, we obtain images in which each pixel has discernible EDS peaks, yielding elemental maps for each sample. The result of this analysis is shown in Figure 5, where the first row shows the signal-averaged HAADF image of the NCs and the following rows show quantified elemental distribution maps for In and Ga. The remaining particle inhomogeneity, imperfect alignment of the particles, and EDS binning limit the resolution of the maps; we cannot resolve the elemental distribution with atomic resolution. Nonetheless, the extensive filtering and alignment give the maps enough fidelity to show the average structure within a representative subset of NCs.

The top row of Figure 5 shows the signal-averaged HAADF for the samples considered, with the number of particles used for signal-averaging displayed at the bottom of the image (see SI, Section 10 and Figure S27 for details). The dashed white lines across the middle indicate where a line profile was taken. The line profiles are shown at the end of the row, where the time in the reaction is indicated from the lightest color ($InP_{1-y}As_y$) to the darkest ($In_{1-x}Ga_xP_{1-y}As_y$ 16 h). The HAADF line profiles reproduce the asymmetric intensity profile of individual ⟨110⟩-oriented particles, shown in Figure 4d. The next row of Figure 5 shows the elemental distribution map for In. Overall, the intensity of the In map drops rapidly from the $InP_{1-y}As_y$ to the $In_{1-x}Ga_xP_{1-y}As_y$ 15 min map and then slowly decreases for the later 3 samples. This abrupt change is reflected in the line profiles, which also show a change in the line shape. While the In composition in the starting material bows down in the middle, after 15 min of molten-salt annealing, the In profile peaks in the middle of the


https://doi.org/10.1021/acsnano.5c15614
ACS Nano XXXX, XXX, XXX−XXX

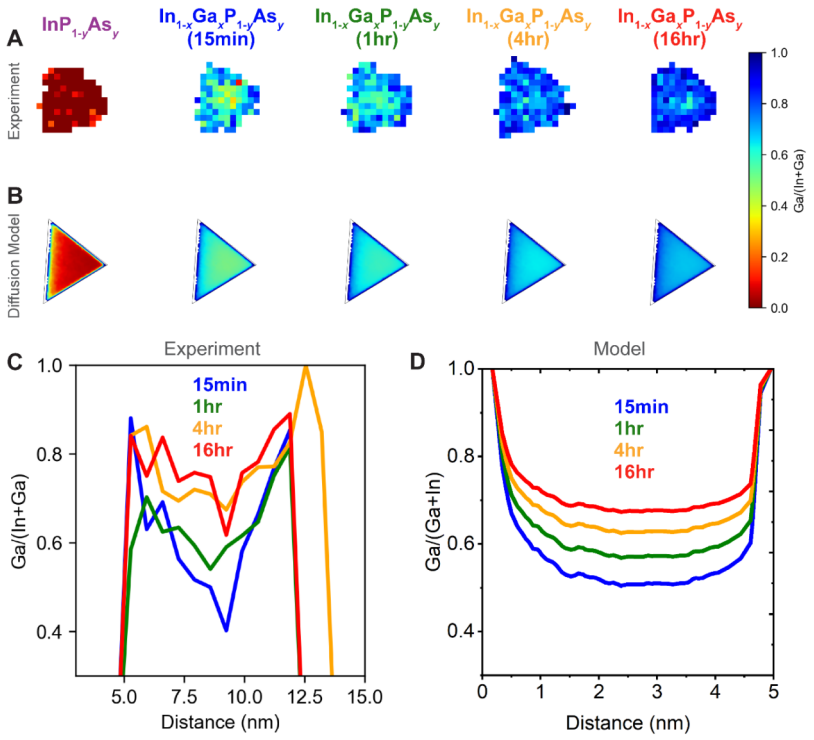


**Figure 6.** (A) Elemental distribution map of the Ga atomic fraction (relative to total In + Ga), determined experimentally from summed particle signal (Figure 5). (B) Modeled composition for ⟨110⟩ oriented tetrahedron, calculated using a composition-dependent diffusion model implemented in COMSOL. The composition is integrated across the thickness of the tetrahedron to account for the experimental measurement being a projection of the NCs. (C) Line profiles of Ga atomic fraction, relative to In + Ga, taken through the middle of the experimental elemental distribution maps. (D) Line profile of Ga fraction from the composition-dependent diffusion model.

map, and that shape remains for the remainder of the reaction. By comparison, the Ga content (third row of Figure 5) is essentially zero for the $InP_{1-y}As_y$ sample and then abruptly increases for the $In_{1-x}Ga_xP_{1-y}As_y$ 15 min map. The Ga content continues to increase, but throughout the exchange, there is a persistent dip in the Ga content in the center of the particles, which is reflected in the maps by a darker spot in the middle and in the line profiles by a dip in the composition. The peak of the In signal and dip in the Ga signal at the center of the particles indicate that the In/Ga composition is nonuniform across particles. The elemental distributions of P and As are shown in SI, Section 10 and Figure S29. The observation of a nonuniform elemental distribution in individual NCs (Figure 4) and the signal-averaged result (Figure 5) suggests that the nonuniform elemental distribution is representative of the sample. We also performed signal averaging without filtering for orientation, which shows a similar nonuniform elemental distribution with lower spatial registration and higher signal (see SI, Section 10 and Figures S30 and S31), providing further evidence that our observations are representative of the sample.

## Modeling Cation Exchange as a Diffusion-Limited Process

In the results shown so far, we observe a rapid transformation at the early stages of the cation-exchange reaction, in which the surface is enriched with Ga, and the cation exchange is less complete inside the particles. Subsequently, despite the reaction proceeding for another 16 h, the changes in the elemental composition are relatively minor, and the In enrichment on the inside of the particle persists. From the standpoint of thermodynamics, one might expect that the cation exchange would eventually replace all the $In^{3+}$ with $Ga^{3+}$ and result in a uniform $GaP_{1-y}As_y$ phase. The standard enthalpies of formation for GaAs and GaP (−87.7 and −103.2 kJ/mol, respectively) are lower than that of InAs and InP (−60.0 and −70.2 kJ/mol, respectively),[51] such that a homogeneous $In_{1-x}Ga_xP_{1-y}As_y$ or pure $GaP_{1-y}As_y$ phase is preferred enthalpically.[23] Furthermore, we expect that the entropy would be maximized for a homogeneous solid solution rather than a graded elemental distribution. The observations of the incomplete exchange and a composition gradient, which ostensibly are neither enthalpically nor entropically preferred, suggest that the cation exchange is kinetically limited. The kinetically limited cation exchange for InAs or InP starting materials in Ga-containing molten salts has been proposed previously, and the key evidence is the persistent observation that higher molten salt annealing temperatures result in faster cation exchange and more Ga-rich compositions.[24,25,27,30]

To examine the kinetic aspects of cation exchange that may impact the resulting elemental distribution, we model the annealing in the molten salt as a diffusion-limited process. To evaluate the elemental distributions that would result from a diffusion-limited process in tetrahedra, we simulated the cation exchange using finite element analysis, implemented in COMSOL Multiphysics (SI, Section 11 and Figure S32). Our simplest model considers the diffusion in a tetrahedron with edge lengths of 7 nm, with a diffusion constant that does not vary during the course of the reaction. We numerically solved the elemental distribution at a series of reaction time points and plotted the projection of the composition in the ⟨110⟩ zone axis. Qualitatively, this model explains some of our experimental observations. From STEM−EDS (Figures 4 and 5), we observed that the edges of the particles exchange before


https://doi.org/10.1021/acsnano.5c15614
ACS Nano XXXX, XXX, XXX−XXX

the core. The model predicts that it takes time for the core to exchange because Ga atoms need to diffuse from the surface to the core. However, the diffusion model with a constant diffusion coefficient struggles to quantitatively reproduce the initially fast but later slow cation exchange. Experimentally, we observe ~50% of In atoms exchange in the first 15 min, yet the exchange fails to complete after 16 h of reacting in the molten salt (Figure 2d). Modeling with a constant diffusion coefficient does not replicate the experimental results; low diffusion coefficients result in the composition change lagging at early times and high diffusion coefficients predict a complete exchange at later times (SI, Section 11 and Figure S33). We then considered a composition-dependent diffusion coefficient: at lower % Ga compositions, it is more favorable for Ga to exchange, while at higher compositions, it is less favorable. This results in a high diffusion coefficient at low compositions, or early times, and a lower diffusion coefficient at higher compositions, or later times (SI, Section 11 and Figures S34 and S35 and surrounding discussion). A linear relationship between the composition and diffusion coefficient still fails to reproduce the experimental results. The diffusion model aligns with the experimental results (Figure 6a,c) when the diffusion coefficient scales as composition to the power of 10 (Figures 6b,d and S35). The large changes in the effective diffusion coefficient with composition that are necessary to explain the data reflect that the rate of cation exchange is substantially different at the early and late reaction times.

To rationalize a cation-exchange rate that drastically slows after a fast initial exchange, we consider previous experimental observations and theoretical predictions. For $Ga^{3+}$ exchange into InP, it was proposed that the initial ensemble composition change is due to rapid surface exchange,[25] and our findings here suggest that this rapid initial change is likely accelerated by the surface *addition* of $Ga^{3+}$. Exchange beyond the surface is thought to be mediated by interdiffusion, a slower process that may be aided by defects, possibly generated and most abundant during the initial surface reconstruction.[24,25,52] The large difference in surface cation exchange and interdiffusion can contribute to the elemental distribution that we observe. These experimental observations may also be explained by theoretical work that shows that local composition influences diffusion rate.[53,54] In particular, the exchange from A → B can be suppressed by the formation of a B-rich shell at the edges of the particle,[54] which in our case would translate to exchange of In at later times being suppressed by the Ga-rich edges of the NC because the lattice contraction induced by smaller Ga atoms suppresses further exchange or diffusion. Additionally, it has been found experimentally that anion composition also impacts diffusion constants: the activation energy of $Ga^{3+}$ diffusion in InP NCs was found to be lower than that in InAs.[24] We tentatively observe that $In_{1-x}Ga_xP_{1-y}As_y$ NCs have P-rich edges and As-rich cores (Figure S29) although the P signal in EDS is weaker than the other elements; therefore, we are less confident in its distribution. In that case, the above-mentioned difference in activation energies would result in faster diffusion through the P-rich edges and slower diffusion through the As-rich cores. Furthermore, there may be specific chemical or strain interactions that would favor the formation of In−As or Ga−P bonds, or the mismatch between Ga−P at the edges and In−As at the core could generate strain that slows exchange. More work is needed to discern which factors have the greatest influence on the rate of diffusion, toward a predictive understanding of how composition and elemental distribution can be controlled as a function of annealing conditions.

Regardless of the mechanisms that lead to the elemental distribution in $In_{1-x}Ga_xP_{1-y}As_y$ NCs, the graded composition may be beneficial to their photophysical properties. Theory suggests that graded interfaces can smooth out the confinement potential and thereby suppress Auger recombination, potentially enhancing photoluminescence quantum yield under high photon flux.[15] Graded II−VI NC compositions have been used to enhance photoluminescence performance.[16−19] The diffusion-limited nature of the molten salt cation exchange could be exploited to form III−V NCs with crystallographically coherent and compositionally graded structures with potentially enhanced photophysical properties. On the other hand, the direct synthesis of III−V alloys in molten salts[28,29] may generate homogeneous elemental distributions, which may lead to different optoelectronic properties with a similar ensemble composition.

## CONCLUSIONS

In this study, we considered the atomistic details of how the cation exchange of $Ga^{3+}$ and $In^{3+}$ occurs in a molten salt medium to produce $In_{1-x}Ga_xP_{1-y}As_y$ NCs. Using HAADF-STEM and STEM-EDS, we characterized the structure and composition of these NCs with a high spatial resolution. Despite large compositional changes, we observe that the tetrahedral morphology (Figure 2) and crystalline structure of the NCs (Figure 3) are largely conserved throughout the exchange. However, there are some subtle changes: the particles slightly increase in size and form sharper facets due to surface reconstruction, and the higher Ga content leads to an overall contraction in the lattice. STEM−EDS data, collected after extensive signal optimization, reveal the changing elemental distribution throughout the exchange. We see that, within several minutes, Ga rapidly deposits and exchanges at the surface of $InP_{1-y}As_y$ NCs, and within hours, Ga exchanges more completely within the nanocrystal (Figure 4). The application of a method to sum EDS signal from many NCs is a critical advancement that enabled the generation of representative composition maps (Figure 5). This revealed a graded elemental distribution within $In_{1-x}Ga_xP_{1-y}As_y$ NCs that gets more but is never completely homogeneous during the course of the reaction. We employed finite element analysis to simulate diffusion-limited exchange, finding that a highly composition-dependent diffusion coefficient is needed to describe the initial fast composition changes at early times but much slower changes at later times (Figure 6). We discussed how this elemental distribution emerges from a diffusion-limited exchange process and how it might impact optoelectronic properties. More broadly, the methods developed here could be used to determine the elemental composition of other colloidal semiconductor NCs. These nanocrystals are typically small (<10 nm) and beam sensitive, which has limited their characterization by electron spectroscopies like EDS and electron energy loss spectroscopy (EELS).

## METHODS

### Synthesis of $InP_{1-y}As_y$, $In_{1-x}Ga_xP_{1-y}As_y$

The $InP_{1-y}As_y$ and $In_{1-x}Ga_xP_{1-y}As_y$ samples were studied in a previous publication, and their synthesis and routine characterization are described there.[28]


https://doi.org/10.1021/acsnano.5c15614
ACS Nano XXXX, XXX, XXX−XXX

### Scanning Transmission Electron Microscopy (STEM)

Aberration-corrected STEM was performed with a Thermo Fisher Scientific Titan Themis operated at accelerating voltages of 80, 200, or 300 kV. Samples were prepared by drop-casting solutions of NCs on ultrathin carbon film TEM grids (Ted Pella, Prod 01824, ultrathin carbon film on lacey carbon support film, 400 mesh, Cu). To minimize air exposure, grids were prepared in a glovebox with an argon atmosphere. After drop-casting, the grids were dried under vacuum in the glovebox antechamber for roughly 30 min, before being transferred back into the glovebox, sealed in an airtight container, and transported to the microscopy facility. Grids were baked at 120 °C under a vacuum overnight to further mitigate contamination. EDS data in Figures 2, 4, 5, and 6 were collected with an accelerating voltage of 80 kV, beam current of roughly 700 pA, and dwell time of 20 $\mu$s, except for one of the large field-of-view maps of $In_{1-x}Ga_xP_{1-y}As_y$ (15 min), which was collected with a beam current of 350 pA. Atomic-resolution HAADF images, shown in Figure 3, were collected with an accelerating voltage of 300 kV.

The analysis and plotting of data were conducted using a series of custom Python scripts, primarily using the open-source library *HyperSpy*.[50] Particle segmentation and morphology measurements were conducted with *ParticleSpy*.[49] See the SI for the full description of the data analysis.

## ■ ASSOCIATED CONTENT

### Supporting Information

The Supporting Information is available free of charge at https://pubs.acs.org/doi/10.1021/acsnano.5c15614.

Additional discussion of quantification of particle size and shape, identification of EDS peaks, absorption spectroscopy, EDS quantification, estimating contribution of surface to composition, crystal structure, and orientation, FFT alignment and radial integration, comparison of FFT and XRD data, analysis of atomic columns in atomic-resolution images, screening STEM-EDS acquisition conditions, investigation of electron dose and beam-induced damage, STEM-EDS signal-averaging, and diffusion modeling using numerical methods. (PDF)

## ■ AUTHOR INFORMATION


### Corresponding Author

**Gordana Dukovic** − *Materials Science and Engineering, University of Colorado Boulder, Boulder, Colorado 80309, United States; Renewable and Sustainable Energy Institute and Department of Chemistry, University of Colorado Boulder, Boulder, Colorado 80309, United States;* orcid.org/0000-0001-5102-0958; Email: gordana.dukovic@colorado.edu

### Authors

**Benjamin F. Hammel** − *Materials Science and Engineering, University of Colorado Boulder, Boulder, Colorado 80309, United States;* orcid.org/0000-0002-9155-9875

**Zirui Zhou** − *Department of Chemistry and James Franck Institute, University of Chicago, Chicago, Illinois 60637, United States;* orcid.org/0000-0001-6740-2432

**Justin C. Ondry** − *Department of Chemistry and James Franck Institute, University of Chicago, Chicago, Illinois 60637, United States;* orcid.org/0000-0001-9113-3420

**Dmitri V. Talapin** − *Department of Chemistry and James Franck Institute, University of Chicago, Chicago, Illinois 60637, United States; Pritzker School of Molecular Engineering, University of Chicago, Chicago, Illinois 60637, United States; Center for Nanoscale Materials, Argonne National Laboratory, Argonne, Illinois 60439, United States;* orcid.org/0000-0002-6414-8587

**Sadegh Yazdi** − *Materials Science and Engineering, University of Colorado Boulder, Boulder, Colorado 80309, United States; Renewable and Sustainable Energy Institute, University of Colorado Boulder, Boulder, Colorado 80309, United States;* orcid.org/0000-0002-3470-9398

Complete contact information is available at: https://pubs.acs.org/10.1021/acsnano.5c15614


### Notes

The authors declare no competing financial interest.

## ■ ACKNOWLEDGMENTS

STEM experiments and analysis were supported by the U.S. National Science Foundation via the STROBE Science and Technology Center under Grant No. DMR 1548924 and carried out at the Facility for Electron Microscopy of Materials at the University of Colorado Boulder (CU FEMM, RRID: SCR_019306). Materials synthesis and simulation were supported by the U.S. National Science Foundation via the Center for Integration of Modern Optoelectronic Materials on Demand (IMOD) Science and Technology Center under Cooperative Agreement No. DMR-2019444. COMSOL simulations were performed using the shared facilities at the University of Chicago Materials Research Science and Engineering Center (MRSEC), supported by the U.S. National Science Foundation under Award Number DMR-2011854. B.F.H. acknowledges support from the U.S. National Science Foundation through the Graduate Research Fellowship Program (NSF-GRFP) under Grant No. DGE 2040434. We thank Prof. Emilie Ringe, Bryce Knutson, Dr. Josh Tailon, and Dr. Lauren Pellows for helpful discussions. We also thank Skylar J. Sherman and Molly Larsen for aiding in the collection of the absorption spectra. The Table of Contents graphic and Figure 1 were made by B.F.H. using Blender (version 4.1) and Adobe Illustrator (version 2022 26.0.3).

## ■ REFERENCES


(1) Geisz, J. F.; France, R. M.; Schulte, K. L.; Steiner, M. A.; Norman, A. G.; Guthrey, H. L.; Young, M. R.; Song, T.; Moriarty, T. Six-Junction III−V Solar Cells with 47.1% Conversion Efficiency under 143 Suns Concentration. *Nat. Energy* **2020**, *5* (4), 326−335.

(2) Chaudhuri, R. G.; Paria, S. Core/Shell Nanoparticles: Classes, Properties, Synthesis Mechanisms, Characterization, and Applications. *Chem. Rev.* **2012**, *112* (4), 2373−2433.

(3) De Trizio, L.; Manna, L. Forging Colloidal Nanostructures via Cation Exchange Reactions. *Chem. Rev.* **2016**, *116* (18), 10852−10887.

(4) Hudry, D.; Backer, A. D.; Popescu, R.; Busko, D.; Howard, I. A.; Bals, S.; Zhang, Y.; Pedrazo-Tardajos, A.; Aert, S. V.; Gerthsen, D.; Altantzis, T.; Richards, B. S. Interface Pattern Engineering in Core-Shell Upconverting Nanocrystals: Shedding Light on Critical Parameters and Consequences for the Photoluminescence Properties. *Small* **2021**, *17* (47), No. 2104441.

(5) Nguyen, H. A.; Dixon, G.; Dou, F. Y.; Gallagher, S.; Gibbs, S.; Ladd, D. M.; Marino, E.; Ondry, J. C.; Shanahan, J. P.; Vasileiadou, E. S.; Barlow, S.; Gamelin, D. R.; Ginger, D. S.; Jonas, D. M.; Kanatzidis, M. G.; Marder, S. R.; Morton, D.; Murray, C. B.; Owen, J. S.; Talapin, D. V.; Toney, M. F.; Cossairt, B. M. Design Rules for Obtaining Narrow Luminescence from Semiconductors Made in Solution. *Chem. Rev.* **2023**, *123* (12), 7890−7952.

(6) Freymeyer, N. J.; Click, S. M.; Reid, K. R.; Chisholm, M. F.; Bradsher, C. E.; McBride, J. R.; Rosenthal, S. J. Effect of Indium Alloying on the Charge Carrier Dynamics of Thick-Shell InP/ZnSe Quantum Dots. *J. Chem. Phys.* **2020**, *152* (16), No. 161104.
(7) Baek, H.; Kang, S.; Heo, J.; Choi, S.; Kim, R.; Kim, K.; Ahn, N.; Yoon, Y.-G.; Lee, T.; Chang, J. B.; Lee, K. S.; Park, Y.-G.; Park, J. Insights into Structural Defect Formation in Individual InP/ZnSe/ZnS Quantum Dots under UV Oxidation. *Nat. Commun.* **2024**, *15* (1), No. 1671.
(8) Hines, M. A.; Guyot-Sionnest, P. Synthesis and Characterization of Strongly Luminescing ZnS-Capped CdSe Nanocrystals. *J. Phys. Chem. A* **1996**, *100* (2), 468−471.
(9) Li, J. J.; Wang, Y. A.; Guo, W.; Keay, J. C.; Mishima, T. D.; Johnson, M. B.; Peng, X. Large-Scale Synthesis of Nearly Monodisperse CdSe/CdS Core/Shell Nanocrystals Using Air-Stable Reagents via Successive Ion Layer Adsorption and Reaction. *J. Am. Chem. Soc.* **2003**, *125* (41), 12567−12575.
(10) Chen, Y.; Vela, J.; Htoon, H.; Casson, J. L.; Werder, D. J.; Bussian, D. A.; Klimov, V. I.; Hollingsworth, J. A. Giant" Multishell CdSe Nanocrystal Quantum Dots with Suppressed Blinking. *J. Am. Chem. Soc.* **2008**, *130* (15), 5026−5027.
(11) Chen, O.; Zhao, J.; Chauhan, V. P.; Cui, J.; Wong, C.; Harris, D. K.; Wei, H.; Han, H.-S.; Fukumura, D.; Jain, R. K.; Bawendi, M. G. Compact High-Quality CdSe−CdS Core−Shell Nanocrystals with Narrow Emission Linewidths and Suppressed Blinking. *Nat. Mater.* **2013**, *12* (5), 445−451.
(12) Fan, F.; Voznyy, O.; Sabatini, R. P.; Bicanic, K. T.; Adachi, M. M.; McBride, J. R.; Reid, K. R.; Park, Y.-S.; Li, X.; Jain, A.; Quintero-Bermudez, R.; Saravanapavanantham, M.; Liu, M.; Korkusinski, M.; Hawrylak, P.; Klimov, V. I.; Rosenthal, S. J.; Hoogland, S.; Sargent, E. H. Continuous-Wave Lasing in Colloidal Quantum Dot Solids Enabled by Facet-Selective Epitaxy. *Nature* **2017**, *544* (7648), 75−79.
(13) Hanifi, D. A.; Bronstein, N. D.; Koscher, B. A.; Nett, Z.; Swabeck, J. K.; Takano, K.; Schwartzberg, A. M.; Maserati, L.; Vandewal, K.; van de Burgt, Y.; Salleo, A.; Alivisatos, A. P. Redefining Near-Unity Luminescence in Quantum Dots with Photothermal Threshold Quantum Yield. *Science* **2019**, *363* (6432), 1199−1202.
(14) Won, Y.-H.; Cho, O.; Kim, T.; Chung, D.-Y.; Kim, T.; Chung, H.; Jang, H.; Lee, J.; Kim, D.; Jang, E. Highly Efficient and Stable InP/ZnSe/ZnS Quantum Dot Light-Emitting Diodes. *Nature* **2019**, *575* (7784), 634−638.
(15) Cragg, G. E.; Efros, A. L. Suppression of Auger Processes in Confined Structures. *Nano Lett.* **2010**, *10* (1), 313−317.
(16) García-Santamaría, F.; Brovelli, S.; Viswanatha, R.; Hollingsworth, J. A.; Htoon, H.; Crooker, S. A.; Klimov, V. I. Breakdown of Volume Scaling in Auger Recombination in CdSe/CdS Heteronanocrystals: The Role of the Core−Shell Interface. *Nano Lett.* **2011**, *11* (2), 687−693.
(17) Bae, W. K.; Padilha, L. A.; Park, Y.-S.; McDaniel, H.; Robel, I.; Pietryga, J. M.; Klimov, V. I. Controlled Alloying of the Core−Shell Interface in CdSe/CdS Quantum Dots for Suppression of Auger Recombination. *ACS Nano* **2013**, *7* (4), 3411−3419.
(18) Park, Y.-S.; Lim, J.; Klimov, V. I. Asymmetrically Strained Quantum Dots with Non-Fluctuating Single-Dot Emission Spectra and Subthermal Room-Temperature Linewidths. *Nat. Mater.* **2019**, *18* (3), 249−255.
(19) Lin, X.; Yang, Y.; Li, X.; Lv, Y.; Wang, Z.; Du, J.; Luo, X.; Zhou, D.; Xiao, C.; Wu, K. Blue Lasers Using Low-Toxicity Colloidal Quantum Dots. *Nat. Nanotechnol.* **2025**, *20* (2), 229−236.
(20) McBride, J. R.; Mishra, N.; Click, S. M.; Orfield, N. J.; Wang, F.; Acharya, K.; Chisholm, M. F.; Htoon, H.; Rosenthal, S. J.; Hollingsworth, J. A. Role of Shell Composition and Morphology in Achieving Single-Emitter Photostability for Green-Emitting "Giant" Quantum Dots. *J. Chem. Phys.* **2020**, *152* (12), No. 124713.
(21) Singh, A.; Majumder, S.; Orfield, N. J. T.; Sarpkaya, I.; Nordlund, D.; Bustillo, K. C.; Ciston, J.; Nisoli, V.; Ivanov, S. A.; Bowes, E. G.; Htoon, H.; Hollingsworth, J. A. From Inside Out: How the Buried Interface, Shell Defects, and Surface Chemistry Conspire to Determine Optical Performance in Nonblinking Giant Quantum Dots. *Small Sci.* **2023**, *3* (11), No. 2300092.
(22) Ahn, N.; Livache, C.; Pinchetti, V.; Jung, H.; Jin, H.; Hahm, D.; Park, Y.-S.; Klimov, V. I. Electrically Driven Amplified Spontaneous Emission from Colloidal Quantum Dots. *Nature* **2023**, *617* (7959), 79−85.
(23) Srivastava, V.; Kamysbayev, V.; Hong, L.; Dunietz, E.; Klie, R. F.; Talapin, D. V. Colloidal Chemistry in Molten Salts: Synthesis of Luminescent $In_{1-x}Ga_xP$ and $In_{1-x}Ga_xAs$ Quantum Dots. *J. Am. Chem. Soc.* **2018**, *140* (38), 12144−12151.
(24) Gupta, A.; Ondry, J. C.; Chen, M.; Hudson, M. H.; Coropceanu, I.; Sarma, N. A.; Talapin, D. V. Diffusion-Limited Kinetics of Isovalent Cation Exchange in III−V Nanocrystals Dispersed in Molten Salt Reaction Media. *Nano Lett.* **2022**, *22* (16), 6545−6552.
(25) Hudson, M. H.; Gupta, A.; Srivastava, V.; Janke, E. M.; Talapin, D. V. Synthesis of $In_{1-x}Ga_xP$ Quantum Dots in Lewis Basic Molten Salts: The Effects of Surface Chemistry, Reaction Conditions, and Molten Salt Composition. *J. Phys. Chem. C* **2022**, *126* (3), 1564−1580.
(26) Gupta, A.; Ondry, J. C.; Lin, K.; Chen, Y.; Hudson, M. H.; Chen, M.; Schaller, R. D.; Rossini, A. J.; Rabani, E.; Talapin, D. V. Composition-Defined Optical Properties and the Direct-to-Indirect Transition in Core−Shell $In_{1-x}Ga_xP$/ZnS Colloidal Quantum Dots. *J. Am. Chem. Soc.* **2023**, *145* (30), 16429−16448.
(27) Ondry, J. C.; Gupta, A.; Zhou, Z.; Chang, J. H.; Talapin, D. V. Synthesis of Ternary and Quaternary Group III-Arsenide Colloidal Quantum Dots via High-Temperature Cation Exchange in Molten Salts: The Importance of Molten Salt Speciation. *ACS Nano* **2024**, *18* (1), 858−873.
(28) Ondry, J. C.; Zhou, Z.; Lin, K.; Gupta, A.; Chang, J. H.; Wu, H.; Jeong, A.; Hammel, B. F.; Wang, D.; Fry, H. C.; Yazdi, S.; Dukovic, G.; Schaller, R. D.; Rabani, E.; Talapin, D. V. Reductive Pathways in Molten Inorganic Salts Enable Colloidal Synthesis of III-V Semiconductor Nanocrystals. *Science* **2024**, *386* (6720), 401−407.
(29) Zhou, Z.; Ondry, J. C.; Liu, Y.-C.; Wu, H.; Jeong, A.; Gupta, A.; Chen, Y.-C.; Chang, J. H.; Schaller, R. D.; Talapin, D. V. Colloidal Chemistry in Molten Inorganic Salts: Direct Synthesis of III−V Quantum Dots via Dehalosilylation of $(Me_3Si)_3Pn$ (Pn = P, As) with Group III Halides. *J. Am. Chem. Soc.* **2025**, *147*, 9198.
(30) Chang, J. H.; Ondry, J. C.; Zangeneh, D.; Zhou, Z.; Gupta, A.; Liu, Y.; Klie, R. F.; Schaller, R. D.; Talapin, D. V. Design of Zn Chalcogenide Shells for Emissive Ga-Rich $In_{1-X}Ga_XAs$ Quantum Dots Synthesized in Molten Salts. *ACS Nano* **2025**, *19* (25), 23096−23104.
(31) Wang, Y.-C.; Slater, T. J. A.; Leteba, G. M.; Roseman, A. M.; Race, C. P.; Young, N. P.; Kirkland, A. I.; Lang, C. I.; Haigh, S. J. Imaging Three-Dimensional Elemental Inhomogeneity in Pt−Ni Nanoparticles Using Spectroscopic Single Particle Reconstruction. *Nano Lett.* **2019**, *19* (2), 732−738.
(32) Slater, T. J. A.; Wang, Y.-C.; Leteba, G. M.; Quiroz, J.; Camargo, P. H. C.; Haigh, S. J.; Allen, C. S. Automated Single-Particle Reconstruction of Heterogeneous Inorganic Nanoparticles. *Microsc. Microanal.* **2020**, *26* (6), 1168−1175.
(33) Wang, Y.; Slater, T. J. A.; Leteba, G. M.; Lang, C. I.; Wang, Z. L.; Haigh, S. J. In Situ Single Particle Reconstruction Reveals 3D Evolution of PtNi Nanocatalysts During Heating. *Small* **2024**, *20* (10), No. 2302426.
(34) Cao, X.; Li, J.; Qian, X.; Li, C.; Peng, X. Nucleation and Growth of Monodisperse and Monocrystalline Wurtzite CdSe Nanocrystals: Zinc Alkanoates as Neutral Ligands. *J. Am. Chem. Soc.* **2025**, *147* (4), 3679−3691.
(35) Kim, K.; Yoo, D.; Choi, H.; Tamang, S.; Ko, J.; Kim, S.; Kim, Y.; Jeong, S. Halide−Amine Co-Passivated Indium Phosphide Colloidal Quantum Dots in Tetrahedral Shape. *Angew. Chem., Int. Ed.* **2016**, *55* (11), 3714−3718.
(36) Kim, Y.; Choi, H.; Lee, Y.; Koh, W.; Cho, E.; Kim, T.; Kim, H.; Kim, Y.-H.; Jeong, H. Y.; Jeong, S. Tailored Growth of Single-Crystalline InP Tetrapods. *Nat. Commun.* **2021**, *12* (1), No. 4454.


https://doi.org/10.1021/acsnano.5c15614
*ACS Nano* XXXX, XXX, XXX−XXX

(37) Cho, E.; Kim, M.; Ouyang, L.; Kim, H.; Bonifas, G.; Coppel, Y.; Nayral, C.; Delpech, F.; Jeong, S. Unraveling the Facet-Dependent Surface Chemistry at Molecular Scale: Photoassisted Oxidation of InP Nanocrystals. *J. Am. Chem. Soc.* **2024**, *146* (46), 31691−31701.
(38) Hirst, L. C.; Kotulak, N. A.; Tomasulo, S.; Abell, J.; González, M.; Yakes, M. K.; Meyer, J. R.; Walters, R. J.; Song, C. Y.; Specht, P.; Ercius, P.; Kisielowski, C. Imaging Atomic-Scale Clustering in III−V Semiconductor Alloys. *ACS Nano* **2017**, *11* (3), 2734−2741.
(39) De Backer, A.; Bals, S.; Aert, S. V. A Decade of Atom-Counting in STEM: From the First Results toward Reliable 3D Atomic Models from a Single Projection. *Ultramicroscopy* **2023**, *247*, No. 113702.
(40) Nasim, W.; Yazdi, S.; Santamarta, R.; Malik, J.; Erdeniz, D.; Mansoor, B.; Seidman, D. N.; Dunand, D. C.; Karaman, I. Structure and Growth of Core−Shell Nanoprecipitates in Al−Er−Sc−Zr−V−Si High-Temperature Alloys. *J. Mater. Sci.* **2019**, *54* (2), 1857−1871.
(41) Lugg, N. R.; Kothleitner, G.; Shibata, N.; Ikuhara, Y. On the Quantitativeness of EDS STEM. *Ultramicroscopy* **2015**, *151*, 150−159.
(42) Frank, J. Advances in the Field of Single-Particle Cryo-Electron Microscopy over the Last Decade. *Nat. Protoc.* **2017**, *12* (2), 209−212.
(43) Azubel, M.; Koivisto, J.; Malola, S.; Bushnell, D.; Hura, G. L.; Koh, A. L.; Tsunoyama, H.; Tsukuda, T.; Pettersson, M.; Häkkinen, H.; Kornberg, R. D. Electron Microscopy of Gold Nanoparticles at Atomic Resolution. *Science* **2014**, *345* (6199), 909−912.
(44) Park, J.; Elmlund, H.; Ercius, P.; Yuk, J. M.; Limmer, D. T.; Chen, Q.; Kim, K.; Han, S. H.; Weitz, D. A.; Zettl, A.; Alivisatos, A. P. 3D Structure of Individual Nanocrystals in Solution by Electron Microscopy. *Science* **2015**, *349* (6245), 290−295.
(45) Azubel, M.; Koh, A. L.; Koyasu, K.; Tsukuda, T.; Kornberg, R. D. Structure Determination of a Water-Soluble 144-Gold Atom Particle at Atomic Resolution by Aberration-Corrected Electron Microscopy. *ACS Nano* **2017**, *11* (12), 11866−11871.
(46) Reboul, C. F.; Heo, J.; Machello, C.; Kiesewetter, S.; Kim, B. H.; Kim, S.; Elmlund, D.; Ercius, P.; Park, J.; Elmlund, H. SINGLE: Atomic-Resolution Structure Identification of Nanocrystals by Graphene Liquid Cell EM. *Sci. Adv.* **2021**, *7* (5), No. eabe6679.
(47) Zhang, H.; Li, X.; Liu, J.; Lan, Y.; Han, Y. Advancing Single-Particle Analysis in Synthetic Chemical Systems: A Forward-Looking Discussion. *Adv. Mater.* **2024**, *36* (51), No. 2406914.
(48) Kang, S.; Kim, J.; Kim, S.; Chun, H.; Heo, J.; Reboul, C. F.; Meana-Pañeda, R.; Van, C. T. S.; Choi, H.; Lee, Y.; Rhee, J.; Lee, M.; Kang, D.; Kim, B. H.; Hyeon, T.; Han, B.; Ercius, P.; Lee, W. C.; Elmlund, H.; Park, J. Time-Resolved Brownian Tomography of Single Nanocrystals in Liquid during Oxidative Etching. *Nat. Commun.* **2025**, *16* (1), No. 1158.
(49) Bell, C. G.; Treder, K. P.; Kim, J. S.; Schuster, M. E.; Kirkland, A. I.; Slater, T. J. A. Trainable Segmentation for Transmission Electron Microscope Images of Inorganic Nanoparticles. *J. Microsc.* **2022**, *288* (3), 169−184.
(50) de la Peña, F.; Prestat, E.; Lähnemann, J.; Fauske, V. T.; Burdet, P.; Jokubauskas, P.; Furnival, T.; Francis, C.; Nord, M.; Ostasevicius, T.; MacArthur, K. E.; Johnstone, D. N.; Sarahan, M.; Taillon, J.; Aarholt, T.; Migunov, V.; Eljarrat, A.; Caron, J.; Nemoto, T.; Poon, T.; Mazzucco, S.; Tappy, N.; Cautaerts, N.; Somnath, S.; Slater, T.; Walls, M.HyperSpy: V2.2.0, 2024. DOI: 10.5281/zenodo.1405741
(51) Yamaguchi, K.; Takeda, Y.; Kameda, K.; Itagaki, K. Measurements of Heat of Formation of GaP, InP, GaAs, InAs, GaSb and InSb. *Mater. Trans., JIM* **1994**, *35* (9), 596−602.
(52) Justo, Y.; Sagar, L. K.; Flamee, S.; Zhao, Q.; Vantomme, A.; Hens, Z. Less Is More. Cation Exchange and the Chemistry of the Nanocrystal Surface. *ACS Nano* **2014**, *8* (8), 7948−7957.
(53) Ott, F. D.; Spiegel, L. L.; Norris, D. J.; Erwin, S. C. Microscopic Theory of Cation Exchange in CdSe Nanocrystals. *Phys. Rev. Lett.* **2014**, *113* (15), No. 156803.
(54) Frechette, L. B.; Dellago, C.; Geissler, P. L. Elastic Forces Drive Nonequilibrium Pattern Formation in a Model of Nanocrystal Ion Exchange. *Proc. Natl. Acad. Sci. U.S.A.* **2021**, *118* (52), No. e2114551118.




https://doi.org/10.1021/acsnano.5c15614
ACS Nano XXXX, XXX, XXX−XXX